Observation of optical coherence in a disordered metal-molecule interface by coherent optical two-dimensional photoelectron spectroscopy

Martin Aeschlimann,[1] Tobias Brixner,[2,3] Mirko Cinchetti,[4,*] Martin Feidt,[1] Norman Haag,[1] Matthias Hensen,[2] Bernhard Huber,[2] Tristan Kenneweg,[5] Jobynson Kollamana,[1] Christian Kramer,[2] Walter Pfeiffer,[5] Stefano Ponzoni,[4] Benjamin Stadtmüller,[1,7] and Philip Thielen[1,6]

[1]*Fachbereich Physik and Research Center OPTIMAS, Technische Universität Kaiserslautern, Erwin-Schrödinger-Str. 46, 67663 Kaiserslautern, Germany*

[2]*Institut für Physikalische und Theoretische Chemie, Universität Würzburg, Am Hubland, 97074 Würzburg, Germany*

[3]*Center for Nanosystems Chemistry (CNC), Universität Würzburg, Theodor-Boveri-Weg, 97074 Würzburg, Germany*

[4]*Department of Physics, TU Dortmund University, 44221 Dortmund, Germany*

[5]*Fakultät für Physik, Universität Bielefeld, Universitätsstr. 25, 33615 Bielefeld, Germany*

[6]*Graduate School of Excellence Materials Science in Mainz, Gottlieb-Daimler-Str. 47, 67663 Kaiserslautern, Germany*

[7]*Institute of Physics, Johannes Gutenberg University Mainz, Staudingerweg 7, 55128 Mainz, Germany*

(Received 17 December 2021; revised 5 April 2022; accepted 6 April 2022; published 10 May 2022)

Coherent multidimensional optical spectroscopy methods overcome some of the limitations found in their one-dimensional counterparts and allow us, for example, to resolve overlapped spectral features, to separate homogeneous and inhomogeneous broadening, and to track the energy transfer kinetics and coherent dynamics in complex quantum systems. In their most common configurations, signal detection is achieved by optical means, making these techniques widespread in studies of bulk systems but less common in the surface and interface sciences. In this paper, we demonstrate an inherently surface-sensitive two-dimensional coherent spectroscopy scheme, based on photoelectron detection, by studying the interface formed between tris(8-hydroxyquinolinato)aluminium (Alq_3) and a ferromagnetic Co surface. Despite the inhomogeneous linewidth broadening ($\approx$800 meV) in the ensemble of disordered molecules, we resolve two narrow resonances ($\approx$10 meV linewidth) with an energy spacing of $\approx$80 meV. By combining experimental data and simulations, using the Lindblad master equation, we identify these resonances as lowest unoccupied molecular orbital (LUMO) to LUMO + 1 transitions in chemically decoupled second-layer Alq_3 molecules and deduce related optical coherence lifetimes of at least 120 and 240 fs. These observations establish that Alq_3 molecules in a disordered adsorbate layer exhibit well-defined and rather homogeneous internal electronic transitions, although the absolute energetic positions of the involved states with respect to the substrate reference are significantly affected by the disorder. The results indicate that inhomogeneous line broadening in a disordered Alq_3 layer and pure dephasing have only a minor impact on optical transitions in individual molecules. This opens interesting opportunities for coherent control schemes and emphasizes the importance of optical coherences for all electron dynamics, even in disordered hybrid metal-molecule interfaces.

DOI: 10.1103/PhysRevB.105.205415

I. INTRODUCTION

Multidimensional optical spectroscopy methods, as introduced more than two decades ago [1–4], are invaluable tools for the investigation of structural, energetic, and dynamical properties of matter. Their application has disclosed the complex photophysics and the dynamics of a broad range of phenomena, including molecular motion in protein folding [5–7], solvation dynamics [8,9], exciton dissociation in photovoltaic thin films [10–12], excitation energy transfer in natural and artificial light-harvesting complexes [13–16], photochemical reactions [17,18], and others [19,20]. The spectral range of multidimensional spectroscopy ranges from the terahertz regime [21,22] over the infrared [5–8] and near-infrared [13–16] to the visible [9–12,17,18] and ultraviolet range [23,24], and potential x-ray applications are discussed [25].

Among the growing number of multidimensional spectroscopy implementations, coherent two-dimensional (2D) vibrational spectroscopy in the infrared spectral range and coherent 2D electronic spectroscopy in the visible spectral range, as it is used in this paper, are by far the most widespread. A 2D spectrum obtained with these methods correlates an excitation energy $\hbar\omega_\tau$ on the one axis with a detection energy $\hbar\omega_t$ on the other axis so that it allows overcoming the issue of spectral congestion [26] common in one-dimensional (1D) pump-probe techniques. The correlation

*mirko.cinchetti@tu-dortmund.de

of excitation and detection energies facilitates researchers to disentangle, e.g., the inhomogeneous and homogeneous contributions to the lineshape of a spectroscopic feature, or to determine the coupling between states in complex systems with multiple interacting components [27]. Such couplings are seen as spectroscopic features at detection energies different from excitation energies, i.e., $\hbar\omega_t \neq \hbar\omega_\tau$. In coherent 2D electronic spectroscopy, these spectra can be recorded by scanning two time delays τ and t which separate three ultrashort optical laser pulses interacting with the system, followed by 2D Fourier transformation of the delay-dependent measurement signal. Moreover, by splitting the second middle pulse into two pulses, it is also possible to introduce an additional intermediate time delay T, the so-called waiting time, that allows one to follow the population evolution of the system on a femtosecond time scale. Formally, the introduction of a systematically varied measurement parameter or any additionally resolved measurement quantity increases the dimensionality of the method so that one generally speaks of multidimensional coherent electronic spectroscopy. Additionally, these methods are sensitive to and can disentangle the types of quantum coherences induced by the interaction with the optical fields [28]. However, the identification of the type of coherence is not always uncontroversial, and some ambiguities arise from the fact that different basis states can be used to describe a quantum system. Here, we follow the discussion in the recent review by Cao *et al.* [16] and define coherences as off-diagonal elements in the density matrix in eigenstate representation. More precisely, following again Cao *et al.* [16], the coherences reported here are optical coherences and reveal upper limits for the homogeneous linewidth of the involved optical transitions in the system.

Despite the outstanding achievements realized with coherent 2D spectroscopies, most of their current implementations, being based on all-optical methods, are intrinsically bulk sensitive. This hinders the applicability of these techniques in many surface-science-related fields, such as molecular electronics and spintronics, where the interaction of a molecular layer with the substrate plays a major role in the emergent physical properties of the system [29–31]. Driven by the necessity to overcome this limitation, surface-sensitive and surface-specific techniques were developed using 2D sum-frequency generation [32–34], total internal reflection [35], or reflection 2D infrared spectroscopy [36]. However, the studies employ infrared pulses for light-matter interaction, therefore restricting the applicability of the respective methods mostly to vibrational transitions and their dynamics.

Here, we demonstrate the applicability of coherent 2D spectroscopy to the electronic structure of a molecular surface system by using photoelectrons of photoemission electron microscopy (PEEM) as the detection channel. Photoemission methods offer intrinsic surface sensitivity due to the short inelastic mean free path of the photoemitted electrons as they propagate toward the surface. We investigate a hybrid interface formed between a Co film and a bilayer of tris-(8-hydroxyquinolinato)aluminum (Alq_3) that is a common component of organic light-emitting diodes and experimental organic spintronic devices [37]. By isolating specific excitation pathways of the surface system from a broad substrate background signal, which is usually dominating the outcome of two-photon photoemission (2PPE) experiments, with the phase-cycling technique of coherent 2D spectroscopy, we detect coherence times on the order of hundreds of femtoseconds at second-layer states of the bilayer and determine upper limits for the homogeneous linewidth of the transitions involved in the process. The existence of such long optical coherence times at a molecular interface is promising for ultrafast all-optical manipulation of molecular optoelectronic devices.

An additional pathway-selective key feature that we employ in this paper is the resolution of the kinetic energy of the emitted photoelectrons. This feature is known from conventional 2PPE spectroscopy [38,39], facilitates the identification of involved electronic states within the surface system, and allows restricting the analysis to a specific set of states involved in the transition. One frequency dimension has been added previously by employing two-pulse excitation followed by Fourier transformation [40]. In this paper, however, we implement the full multipulse 2D spectroscopy pulse sequence and combine it with kinetic energy resolution of detected electrons, leading to another frequency axis, i.e., a full three-dimensional (3D) coherent spectroscopy, which reveals more details about the quantum dynamics. To avoid confusion with population time variation as the third measurement dimension, we refer to our method as coherent optical 2D photoelectron spectroscopy. This term was only recently introduced by Uhl *et al.* [41], who exploited the resolution of the kinetic energy of photoelectrons to study atomic vapors. In this paper, the photoelectron kinetic energy resolution of the acquired 2D spectra reveals that the inhomogeneity of the randomly oriented molecules mainly affects the absolute energy of molecular orbitals (i.e., their alignment with respect to the Co Fermi level), while their relative energy spacing stays rather constant. Note that this additional information channel distinguishes coherent optical 2D photoelectron spectroscopy from, e.g., coherent 2D fluorescence spectroscopy [42–45] that also utilizes a population-based observable. There, the fluorescence yield of molecules is in general exclusively linked to the population of the molecular S_1 state, and hence, no state-selective investigation is possible. Moreover, the presence of a metal can significantly quench molecular fluorescence, and it becomes impossible to discriminate the signal from the background. In contrast, emitted electrons provide an almost background-free detection channel if the delay between pump and coherent probe pulses is adequately chosen.

II. RESULTS

The ultrafast relaxation dynamics of electronic excitations at metal-Alq_3 interfaces depends on the choice of the metal substrate, as was already shown in previous works by, e.g., Ino *et al.* [46] and Min *et al.* [47] for various Cu and Au surfaces. Here, we use ferromagnetic Co as the substrate since, in this hybrid molecular interface, nontrivial spin properties arise due to the complex and tunable molecule-metal interaction [29–31]. We prepare samples by electron beam evaporation epitaxy of 40 monolayers of Co on an Au(111) crystal and subsequent evaporation of $\approx$1.3 nm Alq_3 that forms the

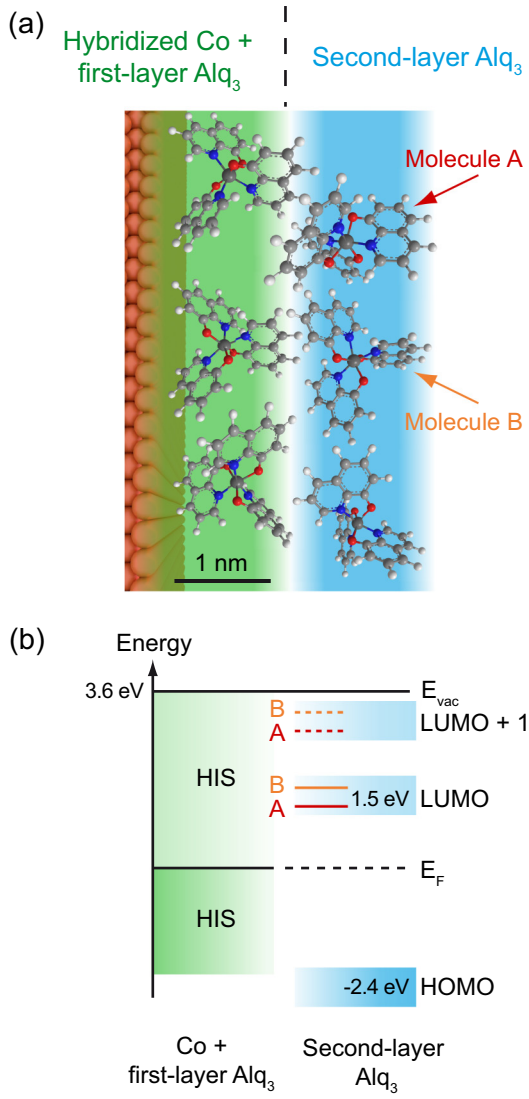

FIG. 1. Schematic representation of the Co-Alq_3 interface. (a) Alq_3 adsorption with two molecular layers: a chemisorbed first layer in direct contact with the surface (green shading) exhibits spectrally broad hybridized interface states (HISs) and a weaker bound second layer retaining its molecular character (blue shading) [48]. Molecule A and B exemplify different orientations of Alq_3 molecules in the second layer. (b) Energy level scheme of Co-Alq_3 for the two-layer configuration [48]. States of individual molecules, e.g., the lowest unoccupied molecular orbitals (LUMOs) of molecules A and B, are shifted in energy with respect to each other (red and yellow, respectively), resulting in an overall inhomogeneous broadening of second-layer energy bandwidths (≈800 meV, shaded areas in blue) as derived from photoelectron spectroscopy experiments [49].

two-layer molecular system, which does not exhibit discernable long-range order, depicted in Fig. 1(a).

The electronic structure of the Co-Alq_3 interface, routinely prepared and previously investigated by some of us [48,49], is shown in Fig. 1(b). The first-layer Alq_3 molecules form a hybridized interface with the Co surface, commonly referred to as hybridized interface states (HISs) [48], and show a broad, metallic density of states arising from the strong chemisorption [green in Fig. 1(b)]. The second-layer Alq_3 molecules are weakly bound to the surface and thus can be described quite well by the molecular orbitals of free Alq_3 molecules. Hence, electronic excitations are mainly localized on individual molecular sites [50], and the molecular orbitals are energetically shifted and broadened due to the weak interaction with neighboring molecules and with the hybridized interface layer [48]. As a consequence, the second-layer molecular features are, in addition to the dissipation-related linewidth, strongly inhomogeneously broadened [indicated as blue-shaded areas in Fig. 1(b)] due to the variation of the relative molecular orientations and screening effects [exemplified by lowest unoccupied molecular orbital (LUMO) levels of molecules A and B in Fig. 1(a)] [51,52]. The 1D method of incoherent 2PPE revealed that the spectral feature of the LUMO state of the second Alq_3 layer, centered at ≈1.5 eV above the Fermi energy (E_F), is strongly broadened by $\Delta E \approx$ 800 meV [48,49]. Note that an 800 meV linewidth of the LUMO corresponds to a coherence lifetime of only ≈1.5 fs.

To investigate coherence effects in both the inhomogeneously broadened LUMO and the energetically higher-lying Alq_3 states of the second layer, we apply pump-pulse-supported coherent optical 2D photoelectron spectroscopy. In this scheme, a pump laser pulse centered at 400 nm (3.1 eV) creates a transient population in the LUMO. As shown in Fig. 1(b), the energy difference between highest occupied molecular orbital (HOMO) und LUMO, $\Delta E_{\mathrm{HOMO–LUMO}} =$ 3.9 eV, exceeds the pump photon energy, i.e., direct excitation within the second molecular layer is not possible. Thus, as shown by Steil *et al.* [49], the LUMO population occurs via the excitation of states in the hybridized Co substrate and first-layer Alq_3 molecules and a direct or indirect charge-transfer process to second-layer molecular states. Acting upon the so-excited state manifold of adsorbed molecules, four pulses centered at 800 nm (1.55 eV, ≈55 fs), illuminating the sample in a collinear geometry (65 ° incidence angle with respect to the surface normal, p polarization), induce and probe the optical coherence. Figure 2(a) shows the two-color excitation pulse scheme. The 400 nm pump pulse always overlaps with the first of the 800 nm probe pulses in space and time, while the other pulses arrive after relative time delays τ, T, and t. By scanning the first time delay τ and the last time delay t, while keeping $T = 0$ fs, we effectively apply a three-pulse sequence. The kinetic-energy-resolved local photoelectron yield is recorded with a PEEM equipped with a time-of-flight delay-line detector [53] (ToF-DLD) resulting in a dataset $Y_{\mathrm{el}}(x, y, \tau, t, E_{\mathrm{kin}})$. In our previous work on coherent 2D nanoscopy [54–56], we have emphasized the value of additional spatial resolution, the key to the disclosure of ultrafast collective electronic dynamics at the nanoscale and therefore to the investigation of plasmonic systems with photoelectronic techniques [57]. In this paper, each image dataset is integrated over the two lateral dimensions x and y over an area of $30 \times 30\ \mu\mathrm{m}^2$ since the sample is, in our case, spatially uniform. The resulting signal $Y_{\mathrm{el}}(\tau, t, E_{\mathrm{kin}})$ can then in principle be converted into kinetic-energy-resolved 2D spectra by performing a Fourier transformation along both τ and t. However, such an evaluation comprises all possible excitation pathways in the Liouville space of the system. To select and analyze specific excitation pathways in our collinear excitation geometry, we record the signal $Y_{\mathrm{el}}(\tau, t, E_{\mathrm{kin}})$ for

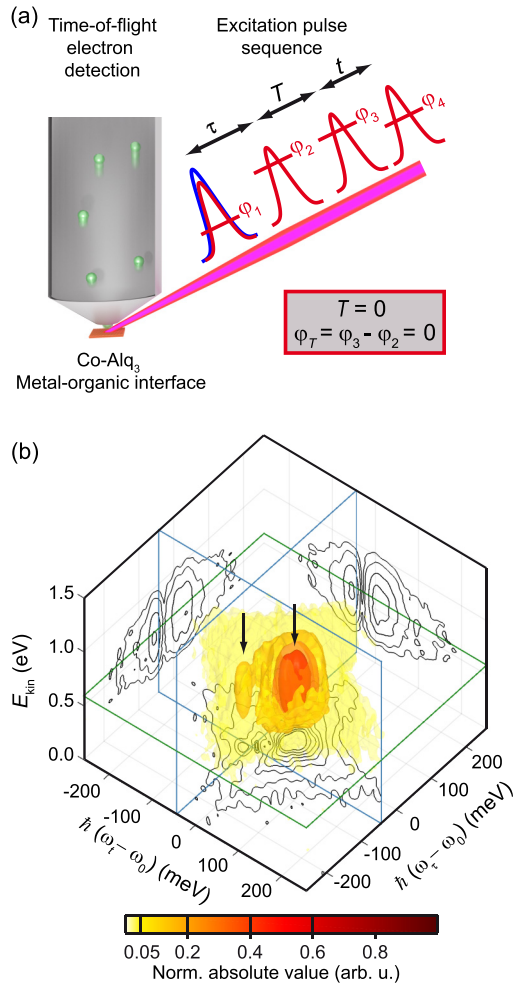

FIG. 2. Coherent optical two-dimensional (2D) photoelectron spectroscopy. (a) Excitation scheme consisting of a 400 nm (3.1 eV) pump pulse and a collinear sequence of four 800 nm (1.55 eV) probe pulses. The second and third pulses are kept in temporal overlap ($T = 0$ fs) in this experiment, resulting in an effective three-pulse sequence, while the time delays τ and t and relative phases $\varphi_\tau = \varphi_2 - \varphi_1$ and $\varphi_t = \varphi_4 - \varphi_3$ are scanned. 2D Fourier transformation with respect to τ and t yields a 2D spectrum with axes for the excitation energy $\hbar(\omega_\tau - \omega_0)$ and detection energy $\hbar(\omega_t - \omega_0)$, centered at the energy of the probe laser photons at $\hbar\omega_0 = 1.55$ eV. (b) Normalized absolute-value part of the retrieved three-dimensional (3D) spectroscopic data for reverse-transient-grating-equivalent phase cycling $|S_{\mathrm{RTG}}[\hbar(\omega_\tau - \omega_0),\ \hbar(\omega_t - \omega_0), E_{\mathrm{kin}}]|$, consisting of 2D spectra as a function of the electron kinetic energy. Two distinct peaks are visible (black arrows), corresponding to two transitions in the Alq_3 state manifold, and they persist over the entire range of the observed electron spectrum from 0.1 to 1.1 eV. Hence, without the coherent multipulse excitation scheme spanning the excitation energy and detection energy axes, these transitions would be obscured in the electron spectrum by an inhomogeneous broadening of > 0.8 eV. Isovalues of plotted surfaces are indicated inside the color bar by black tick lines. The green plane at $E_{\mathrm{kin}} = 0.6$ eV illustrates the cut position of the 2D spectrum shown at the bottom of the data cube (black contour lines) and in Fig. 3(d). Blue planes indicate cuts along constant $\hbar(\omega_\tau - \omega_0) = -0.43$ meV and $\hbar(\omega_t - \omega_0) = -0.43$ meV that are shown on the back right and left planes, respectively (black contour lines). The contour lines of all cuts are drawn at values of 0.05, 0.1, 0.2, 0.3, 0.4, 0.5, 0.6, and 0.7.

a corresponding set of relative phases ($\varphi_t = \varphi_2 - \varphi_1$, $\varphi_t = \varphi_4 - \varphi_3$) between the pulses, where φ_j, $j = 1, \ldots, 4$, indicates the absolute offset phase of pulse number j. The relative phase between the second and third pulse $\varphi_T = \varphi_3 - \varphi_2$ is set to zero throughout the experiment. By taking an appropriate linear combination of the datasets $Y_{\mathrm{el}}(\tau, t, \varphi_\tau, \varphi_\tau, E_{\mathrm{kin}})$ collected with different values of the relative phases according to the phase-cycling technique [58] and subsequent Fourier transformation along τ and t for each constant kinetic energy slice, the linear background is filtered out, and only the kinetic-energy-resolved 2D spectrum $S(\hbar\omega_\tau, \hbar\omega_t, E_{\mathrm{kin}})$, ascribable to a defined set of excitation pathways, is retained. We choose a $1 \times 3 \times 4 = 12$-fold phase-cycling scheme and extract the contribution with the same phase dependence as the so-called reverse transient grating (RTG) [59] in conventional noncollinear coherent 2D electronic spectroscopy (see Materials and Methods). Note that we use the term RTG in our studies even though transient grating is commonly associated with a noncollinear measurement geometry. Nevertheless, since we obtain analogous response contributions from phase cycling, we employ this term in accordance with a phase-cycling overview by Tan [58], who linked the signal contributions of phase-matched noncollinear coherent 2D experiments to those obtained by phase cycling. This signal $S_{\mathrm{RTG}}(\hbar\omega_\tau, \hbar\omega_t, E_{\mathrm{kin}})$ belongs to a set of various nonrephasing pathways in which the coherence between LUMO states of the molecule evolves during the time intervals τ and t. Note that there is no fixed phase relation between the 400 nm pump pulse and the sequence of 800 nm probe pulses. The sample coherence is only investigated via the ≈800 nm probe pulse sequence interacting with the optically pumped molecules. Using the RTG phase-cycling scheme instead of the rephasing photon-echo phase-cycling scheme—that additionally would allow us to directly read homogeneous and inhomogeneous line widths from 2D spectra—might seem inconvenient. However, when applying the 16-fold photon-echo phase-cycling scheme, we noticed unphysical signals that extended over the entire diagonal of 2D spectra, an artifact that we have discussed previously [60] and which results from pixel-to-pixel crosstalk in the spatial light modulator (SLM) inside the pulse shaper. We therefore pragmatically applied the 12-fold phase-cycling scheme since the retrieved signal shows no sign of artifact contamination, and it can likewise be used to probe the coherence between molecular states.

We stress that, by employing a sequence of four collinear pulses with the phase-cycling technique, our excitation scheme allows the full characterization of the nonlinear optical response function of the sample, in analogy with all-optical four-wave mixing techniques like noncollinear coherent 2D electronic spectroscopy [54,61]. The formal difference lies in the signal detection: In conventional 2D spectroscopy techniques, the sample emits a coherent signal field in a phase-matched direction after n interactions with the noncollinear pulse sequence, while in our case, the system resides in a population, i.e., a photoemission state, after $n + 1$ interactions with the collinear pulse sequence. Although the detection of coherent and incoherent observables seems to be quite different, both methods systematically map out the nth order nonlinear response function. Although there are some differences in the 2D lineshapes and the interpretation

of cross-peaks, analyzing the Liouville space pathways shows that a response function of nth order with coherent detection corresponds to an $(n+1)$th order perturbation expansion with population detection [61–63].

Figure 2(b) shows the absolute-valued kinetic-energy-resolved 2D spectrum $|S_{\mathrm{RTG}}[\hbar(\omega_\tau-\omega_0),\ \hbar(\omega_t-\omega_0), E_{\mathrm{kin}}]|$, i.e., the correlation of the optical excitation energy $\hbar(\omega_\tau-\omega_0)$ and optical detection energy $\hbar(\omega_t-\omega_0)$ with respect to the central laser frequency ω_0 corresponding to the 800 nm pulse sequence, i.e., the 2D spectra as a function of the photoelectron kinetic energy E_{kin}. Two separated peaks [black arrows in Fig. 2(b)] exist in the 2D spectra, which persist over the entire observed kinetic energy range. These two kinetic-energy-independent features can be clearly seen in both vertical cross-sections through the full 3D data cube shown in Fig. 2(b), displayed as contour-line plots in the corresponding Cartesian planes for constant excitation energy of $\hbar(\omega_\tau-\omega_0)=-43$ meV (back right plane) and at a constant detection energy of $\hbar(\omega_t-\omega_0)=-43$ meV (back left plane). Interestingly, the linewidths of the peaks in the 2D spectrum at a kinetic energy of $E_{\mathrm{kin}}=0.6$ eV, displayed as a contour plot at the bottom plane of the 3D cube, are much narrower ($\approx$10 meV) than the inhomogeneously broadened absorption profile ($\approx$800 meV) retrieved from incoherent 2PPE spectra in previous studies [48,49]. Furthermore, the appearance of a substructure of two peaks indicates that the inhomogeneously broadened spectral feature seen in incoherent 2PPE [49] is composed of inhomogeneous contributions from multiple states that are involved in the excited-state dynamics of Alq_3 molecules. Note, as it will become evident in the discussion, that the lack of variance of the spectral features for different final-state kinetic energies is a key feature of the observed kinetic-energy-resolved 2D spectrum that is essential for identifying the underlying excitation mechanism.

To further analyze the origin of the observed features, we deduce the multiphoton order n of the photoemission process, as this limits the number of possible excitation pathways. For this purpose, we perform power law measurements (see Supplemental Material [64]), i.e., we measure the photoemission yield as a function of the incident laser power. Figure 3(a) (top panel) shows the result for constant 400 nm pump power and varying power of an 800 nm single probe pulse in spatial and temporal overlap. The fit of a power law dependence to the data retrieves a multiphoton order of $n_{800\,\mathrm{nm}}=1.05\pm0.05$; hence, the photoemission yield scales linearly with the incident laser power. In a similar manner, the case of constant 800 nm single-probe-pulse power (fluence $<1.0\times10^{-4}$ J cm^{-2}) and varying 400 nm pump-pulse power yields $n_{400\,\mathrm{nm}}=1.12\pm0.07$, i.e., again a dominantly linear dependence (see Fig. S1(b) in the Supplemental Material [64]). In addition to the static power law experiments, we deduce the linear dependence of the signal yield on the probe-pulse intensity also from time-resolved pump-probe experiments using a pair of 800 nm probe pulses (see Supplemental Material [64]).

III. DISCUSSION

Any conceivable model for light-matter interaction at the Co-Alq_3 interface must consider the experimental results described above, i.e., the linear dependence of the photoemission process with respect to probe and pump pulse power, and the narrow spectral features of the 2D spectrum which persist over the entire observed kinetic energy range of photoelectrons. First, we discuss the power dependence of the photoemission process. As one conceivable model, the dashed arrows in Fig. 3(b) show a trivial scheme that might be envisioned to explain the linear power dependence for the pump and the probe step: In that scenario, a pump-induced hot electron population in Co and first-layer Alq_3 HIS would be probed with the 800 nm probe pulse [blue and red dashed arrows in Fig. 3(b)]. However, this scheme cannot explain the observation of narrow spectral features in kinetic-energy-resolved 2D spectra [Fig. 2(b)] because rapid dephasing at the hybridized interface would lead to significantly broadened peaks that are not observed. Thus, for modeling the data, the interplay of the Co substrate and the weakly bound second-layer Alq_3 molecules in the excitation scheme is crucial. Note that any attempt at modeling the almost linear power dependence with respect to the 800 nm excitation based on a coherent coupling of the second-layer LUMO states to continuum photoemission states ($|\mathrm{PE}\rangle$) failed to reproduce the observed 2D spectra. Only one model that relies on an Auger-like energy transfer mechanism succeeded and is shown in Fig. 3(b) (solid arrows). Note that we employ the term photoemission throughout this paper since, here, the Auger emission occurs from a photon-excited state.

The derived model is now explained in detail. Following the experimental findings of Steil *et al.* [49], the 400 nm pump pulse [right solid blue arrow in Fig. 3(b)] induces an Alq_3 LUMO population by optical excitation from the hybridized Co substrate and first Alq_3 layer ($|\mathrm{HIS0}\rangle\rightarrow|\mathrm{HIS1}\rangle$) and subsequent charge injection into the LUMO (state $|1\rangle$) in the second Alq_3 layer (dotted purple arrow). In parallel, the blue pulse also excites a higher lying state $|\mathrm{X}\rangle$ either in the first or second Alq_3 layer [left solid blue arrow in Fig. 3(b)]. One of these 400 nm excitations is close to saturation, presumably the pump process of the LUMO state, explaining the just slightly nonlinear power law for the 400 nm excitation with the multiphoton order $n_{400\,\mathrm{nm}}=1.12\pm0.07$. Then the probe-pulse sequence induces a coherence between the LUMO (state $|1\rangle$) and the LUMO + 1 (states $|2\rangle$ and $|3\rangle$), indicated with the solid red double arrow in Fig. 3(b). The two spectral features observed in the experimentally retrieved kinetic-energy-resolved 2D spectrum, visible for all kinetic energies [Fig. 3(c)], thus correspond to $|1\rangle\leftrightarrow|2\rangle$ and $|1\rangle\leftrightarrow|3\rangle$ transitions. To support an electron emission process in this excitation scheme, the coherence driven between the LUMO and the LUMO + 1 states is converted into a population of the LUMO + 1 states by the last interaction within the probe-pulse sequence. To obey the observed linear order of the emission process, energy released from the decay of the LUMO + 1 population is transferred via an Auger-like mechanism to the excited $|\mathrm{X}\rangle$ state in either the first or the second Alq_3 layer [orange arrows in Fig. 3(b)]. From this $|\mathrm{X}\rangle$ state in either layer, the continuum can be reached with 1.55 eV excitation energy, and thus, the transferred energy leads to electron emission. Note that the excited state $|\mathrm{X}\rangle$ must be in the vicinity of the Alq_3 molecule in which the LUMO state was initially pumped to ensure an efficient

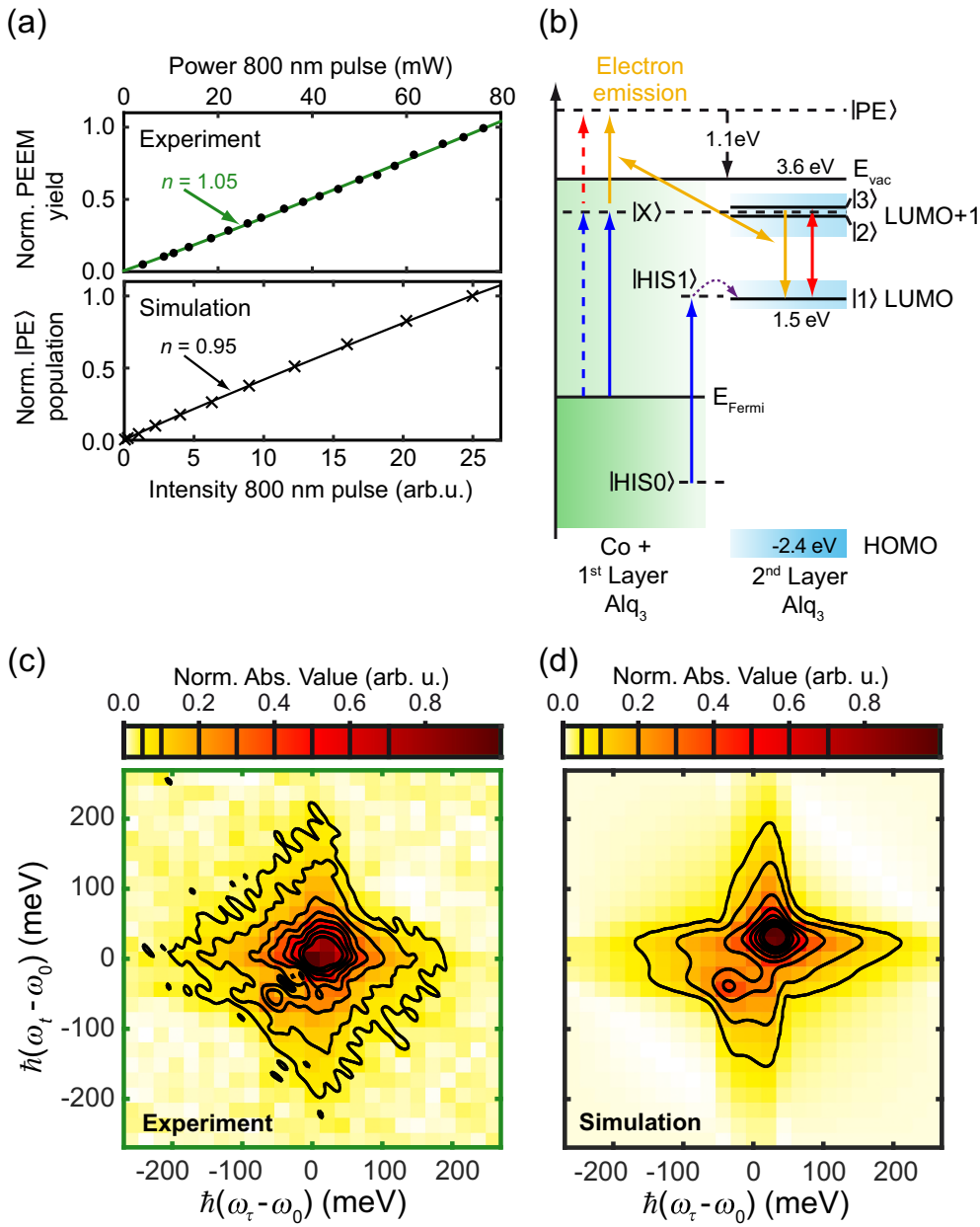

FIG. 3. Comparison of experimentally retrieved kinetic-energy-resolved two-dimensional (2D) spectrum with model simulation. (a) Top: Single-probe-pulse power dependence (black symbols) of the photoemission yield from the Co-Alq_3 interface at constant pump-pulse power of 1 mW (fluence $< 1.4 \times 10^{-6}$ J cm^{-2}, see Experimental Method section) at zero delay time, with power law fit (green) and the extracted multiphoton order n. Bottom: Simulated photoemission signal probe intensity dependence for the model represented in B along with power law fit (line) and multiphoton order n. (b) Energy diagram and excitation scheme of direct two-color photoemission in the hybridized Co and first-layer Alq_3 molecules (dashed arrows, unsuccessful trivial model) and for the proposed applicable model (solid arrows) based on an Auger-like energy transfer (solid orange arrows) leading to electron emission from state $|X\rangle$ into state $|PE\rangle$. The blue solid arrow indicates the pump-pulse excitation and the red solid arrow the probe-pulse-sequence interactions. (c) Absolute value of the experimental kinetic-energy-resolved 2D spectrum at the highest signal magnitude [$E_{kin} = 0.6$ eV, cut at green plane in Fig. 2(b)]. (d) Simulated 2D spectrum ($E_{kin} = 0.6$ eV) based on the model shown in (b) with time delays and phase cycling equivalent to the experiment. For both 2D spectra, the pixel size underneath the contour lines indicates the spectral resolution in experiment and simulation, while the contour lines result from zero-padded data.

Auger-like energy transfer. We would like to point out that the rearrangement of excited electronic configurations, in which the energy of the de-excitation of one electron is converted into the excitation of another electron, is a well-known process in time-resolved photoelectron spectroscopy [65,66]. If the excited state $|X\rangle$ lies close to the vacuum potential, as in our case, an electron can be emitted in an Auger-like process. Ionization caused by the electronic relaxation of a neighboring molecule is a common and extensively studied nonlocal decay mechanism, termed intermolecular Coulombic decay, which

can take place within only a few femtoseconds [67]. It is even conceivable that state $|X\rangle$ is in the same molecule. However, in that case, the increased energy transfer efficiency would be balanced by the lower probability of a double excitation in the same molecule than another excitation in the vicinity.

One key aspect of the coherent optical 2D photoelectron spectroscopy scheme is that spectral features of the induced system dynamics can, in principle, be assigned to specific molecular states due to the kinetic energy resolution of photoelectrons. Here, irrespective of the disorder of Alq_3 molecules at the interface and the previously measured inhomogeneous broadening of ≈800 meV of LUMO(+1) states in incoherent 2PPE experiments, we observe that the narrow linewidths of ≈10 meV of the two spectral features, as well as their spectral position, is maintained in the 2D spectra for a continuous range of kinetic energies up to $E_{kin} = 1.1$ eV [Fig. 2(b)]. This implies that the states involved in the respective transitions exhibit both the character of individual molecules, i.e., a rather narrow linewidth, as well as similar transition energies. Hence, we conclude that the relative energies of states involved in the LUMO-to-LUMO + 1 transitions, which are according to our model coherently driven by the multipulse sequence, stay constant, while disorder-induced inhomogeneity mainly affects the absolute state energies of individual molecules. This absolute shift of state energies (with respect to the Co Fermi level) leads to a broad excited-state manifold of $|X\rangle$ and hence to a large range of kinetic energies for which the narrow spectral features are observed. We draw only one possible state of the $|X\rangle$ manifold in Fig. 3(b) that leads to the highest kinetic energy of the final state $|PE\rangle$. The maximum kinetic energy of photoelectrons is given by the substrate Fermi level and the subsequent absorption of a single pump and a single probe photon. Note that we do not expect spectral diffusion to have a significant influence on our experiment, as will be discussed below.

To test the proposed model in comparison with experimental data, we perform simulations by numerically solving the Lindblad quantum master equation and propagating the density matrix in the time domain upon interaction with external laser pulses. We set the time delays and phase combinations like in the experiment (see Materials and Methods). The population in the photoemission state $|PE\rangle$, accumulated over the simulation time, defines the simulated photoemission yield. As a first step, we evaluate the probe-pulse power law dependence. Figure 3(a) (bottom panel) shows the simulated electron yield as a function of probe-pulse intensity. In agreement with experimental observation (top), the model exhibits a linear dependence of the electron yield on laser power with a multiphoton order of $n = 0.95 \pm 0.01$. Next, we explain the numerical model in more detail and apply it to the coherent optical 2D photoelectron spectroscopy scheme.

We simulate a 2D spectrum at the specific kinetic energy of maximum signal intensity ($E_{kin} = 0.6$ eV) of the full kinetic-energy-resolved 2D spectrum and optimize the model parameters to match the experimental data. The restriction to simulate a 2D spectrum at a specific kinetic energy is based on the conclusion that the disorder-induced inhomogeneity only affects the absolute energy of states while their energy spacing stays rather constant. Hence, all molecules are expected to produce a similar 2D spectrum, while the variable absolute energy of states only results in a different kinetic energy of the Auger-emitted electron from $|X\rangle$. All energy levels are defined with respect to the Fermi energy E_F and, correspondingly, $E(|HIS0\rangle) = -1.60$ eV and $E(|HIS1\rangle) = 1.50$ eV. The energy levels in Alq_3 molecules in the second layer, $E(|n\rangle)$ with $n \in \{1, 2, 3\}$, are deduced from a phenomenological fit model of two Lorentzian oscillators to the kinetic-energy-integrated 2D spectrum (see Supplemental Material [64]) and the previously measured energetic peak positions of the LUMO state [51], yielding $E(|1\rangle) = 1.50$ eV, $E(|2\rangle) = 3.01$ eV, and $E(|3\rangle) = 3.09$ eV. The interaction of these three states with the multipulse probe sequence is treated using a Lindblad master equation for the quantum system (see Materials and Methods). In addition, our model requires an occupied excited state $|X\rangle$, pumped with the 400 nm pulse, from which the electron is emitted in an Auger-like process. Its energy is irrelevant in the present simulation since there is no coherent coupling to other states, and its population change is treated using rate terms in the master equation.

To model the temporal dynamics of the system, all involved states require appropriate time constants in the Lindblad formalism. These are the population relaxation time T_1 and the pure dephasing time T_2^*. Both contribute to the decoherence time T_2, which is essential for the coherent interaction with external light fields:

$$\frac{1}{T_2} = \frac{1}{2T_1} + \frac{1}{T_2^*}. \tag{1}$$

To keep the parameter space as small as possible for optimization procedures, we make the following assumptions: Pure dephasing times of $T_2^* = 0.1$ fs are assigned to the states $|X\rangle$ and $|PE\rangle$ to account for the metal character of the substrate and for a state above the vacuum potential, respectively. In contrast to that, we do not consider pure dephasing of the states $|1\rangle$, $|2\rangle$, and $|3\rangle$ of second-layer Alq_3 molecules that interact with the multipulse probe sequence. This is because the experimental investigation of T_2^* times requires the scanning of the waiting time T, which was kept constant at $T = 0$ fs in our experiments. Note that the same is true for spectral diffusion. The reason for not scanning T is that, in our experiment, it takes approximately one day of measurement time to record a single T step. Consequently, it would not have been possible to maintain comparable experimental conditions for longer than one day of continuous measurement with the present setup. However, we assume that both phenomena have a minor contribution to the linewidths of the spectral features, as will be justified below. Hence, the only free parameters in the simulation are the population relaxation times $T_1(|1\rangle)$ of the LUMO, $T_1(|2\rangle)$ and $T_1(|3\rangle)$ of the LUMO + 1 states, and $T_1(|X\rangle)$. The parameters are varied systematically (see Materials and Methods) to obtain a good match between the simulated 2D spectrum [Fig. 3(d)] and the measured 2D spectrum at the specific kinetic energy of $E_{kin} = 0.6$ eV [Fig. 3(c)]. By comparing the simulated spectra with experimental data, we find the set of values giving the smallest root-mean-square deviation from the measurement.

Figure 3(d) shows the resulting absolute-valued simulated 2D spectrum of the RTG contribution, which is in very good agreement with the experimental observation in Fig. 3(c). The lowest root-mean-square deviation is found for $T_1(|X\rangle) =$

100 fs. Since long-lived states in Co are not known [68], this rather long lifetime for a highly excited state excludes the option that an excited Co state acts as an initial state for this Auger-like emission process. However, both in the first and second layer, excited states with such lifetimes are conceivable. Of great interest are the extracted population relaxation times of the LUMO and LUMO + 1 states in the second layer for which we obtain $T_1(|1\rangle) = 300$ fs, $T_1(|2\rangle) = 75$ fs, and $T_1(|3\rangle) = 200$ fs. Note that these values are given without uncertainty margins since a complete statistical analysis of the parameter space is beyond our computational means. However, the values provide a reliable order-of-magnitude estimate since significant changes in these values lead to significant discrepancies between measured and simulated 2D spectrum.

The rather long lifetimes of the Co-Alq_3 interface states $|1\rangle$, $|2\rangle$, and $|3\rangle$ are not completely unexpected. The obtained population relaxation time $T_1(|1\rangle) = 300$ fs is in good agreement with the value determined from time-resolved incoherent 2PPE measurements [49] that revealed spin-dependent population relaxation times between 400 and 800 fs for majority and minority electrons, respectively. This agreement between independent experiments also renders the population relaxation times for the states $|2\rangle$ and $|3\rangle$ as reliable. Note that these times are exclusively accessible with the here-presented experimental scheme and not from conventional 2PPE measurements since the signal at the final-state energy of the $|2\rangle$ and $|3\rangle$ manifold is dominated, in conventional 2PPE experiments, by the contributions from the Co substrate [49]. We isolate the signal of the almost resonantly driven $|1\rangle \leftrightarrow |2\rangle$ and $|1\rangle \leftrightarrow |3\rangle$ transitions from the undesired incoherent Co background by the excitation pathway selection introduced by the phase-cycling procedure.

According to Eq. (1), the retrieved population relaxation times represent lower limits, and they can, in principle, be slightly longer. For instance, if we assume $T_1 = 400$ fs, as retrieved from conventional 2PPE experiments [49], a pure dephasing time of $T_2^* = 2.5$ ps is required to give the same decoherence time T_2, like in our model, in which this time is solely determined by T_1. Comparing these time scales, the population relaxation seems to be the major contribution to the linewidths of the spectral features in the 2D spectra. Hence, although we cannot clearly differentiate between different contributions to linewidths, due to the constant waiting time $T = 0$ fs in our multipulse sequence, the rather good agreement between the $T_1(|1\rangle)$ reported here and the independent population lifetime measurements [49] indicates that pure dephasing processes, spectral diffusion, and other processes leading to an inhomogeneous broadening of the LUMO-LUMO + 1 transitions, i.e., the relative energy shift of LUMO states, play only a minor role.

Having justified the approximation of the absence of pure dephasing, we now determine the lifetime T_2 for the decay of the optical coherence between states $|1\rangle$ and $|2\rangle$ as well as between the states $|1\rangle$ and $|3\rangle$ via $T_2(|1\rangle \leftrightarrow |2\rangle) = 2[T_1^{-1}(|1\rangle) + T_1^{-1}(|2\rangle)]^{-1}$ and $T_2(|1\rangle \leftrightarrow |3\rangle) = 2[T_1^{-1}(|1\rangle) + T_1^{-1}(|3\rangle)]^{-1}$, respectively. The time constants $T_1(|1\rangle)$, $T_1(|2\rangle)$, and $T_1(|3\rangle)$ are the corresponding population relaxation times. This yields the lower limits for the optical coherence lifetime of the here-probed electronic transitions as $T_2(|1\rangle \leftrightarrow |2\rangle) = 120$ fs and $T_2(|1\rangle \leftrightarrow |3\rangle) = 240$ fs. For pure dephasing absent, the full width at half maximum linewidth Γ of an optical transition is given by $\Gamma = 2\hbar/T_2$, yielding ≈11 and 5.5 meV for the low- and high-energy LUMO-LUMO + 1 transitions probed, respectively. Here, these values for the linewidth are upper bounds for the actual homogenous linewidth since these values can still be affected by inhomogeneous line broadening. The observed upper limit for the homogeneous linewidth sets a bound for possible intralayer coherent energy transfer mechanisms that can become highly relevant if ultrafast dynamics in such films are considered, for example, in a carrier injection or charge separation process at such an interface.

Lastly, we examine the origin of the closely spaced peaks which we associate with the 80 meV energy spacing of the states $|2\rangle$ and $|3\rangle$ in Fig. 3(b) and for which both electronic and vibrational origins are conceivable. Concerning the former, it is known from the literature [69] that the LUMO and LUMO + 1 in Alq_3 are composed of closely spaced levels with an energy separation of ≈100 meV [48] (calculated for the LUMO states of second-layer molecules on Co), which is in accordance with the energy difference of 80 meV observed here. In addition, calculated homogeneous LUMO linewidths of 3–6 meV [48] are in close accordance with the values derived from our models. As a second possible explanation for the observed states, vibrational transitions are conceivable since a skeletal in-plane vibration at 534 cm^{-1} (66 meV), mainly localized on the a-quinolate ligand, was previously identified by density functional theory calculations [50]. A matching mode was observed experimentally with Raman spectroscopy in powdered Alq_3 samples at low temperatures [70]. Both possible candidates for energy levels in the second-layer Alq_3 molecules, either electronic or vibrational, make the observed level structure in coherent optical 2D photoelectron spectroscopy plausible, and vibronic mixing effects [71] may also be relevant.

IV. CONCLUSIONS

In conclusion, we applied coherent optical 2D photoelectron spectroscopy which connects the correlation of excitation and detection energies of conventional coherent 2D electronic spectroscopy with the kinetic energy resolution of emitted electrons. The surface sensitivity, due to the photoelectron detection, allowed us to study the coherent electron dynamics in the unoccupied state manifold of a ferromagnetic metal-molecular interface, previously populated by an additional pump pulse. Our findings demonstrate long-lived optical coherence up to 240 fs in the ensemble of disordered, second-layer molecules of the hybrid Co-Alq_3 interface. Despite the inhomogeneous arrangement of molecular orientations and couplings to the environment, our measurements reveal rather small linewidths of the involved excitations (≈10 meV). Since the small linewidths persist throughout the entire range of kinetic energies of emitted electrons, we conclude that the respective transition energies stay rather constant for individual molecules and that disorder only affects absolute state energies. With our analysis, based on a Lindblad quantum master

equation, we find that the coherent dynamics of two LUMO-LUMO + 1 transitions in the second Alq_3 layer can only be probed and mapped onto experimental data via an Auger-like electron emission process. Candidates for the two narrow excited-state energy levels have either electronic, vibrational, or mixed vibronic character. Independent of that, the observed long coherence times are attributed to a superposition of states in two electronic level manifolds, LUMO and LUMO + 1, and they thus arise from an optical coherence centered at 800 nm. Our findings pave the way to the systematic investigation of coherence effects on the electron dynamics at hybrid molecular interfaces. We envision that the manipulation of these coherences, via pulsed laser excitation, could lead to the development of spintronic and molecular electronic devices where the function of the organic layer is manipulated on a femtosecond time scale in a coherent nondissipative fashion.

V. MATERIALS AND METHODS

A. Sample preparation

Experimental results were obtained from an Au(111)/Co/Alq_3 sample prepared in an ultrahigh vacuum chamber. The system consists of two evaporation chambers for Co and Alq_3 with base pressures of 3×10^{-11} and 2×10^{-9} mbar, respectively, and a PEEM chamber with a base pressure of 9×10^{-11} mbar. The Au crystal was first prepared by several Ar-ion sputtering and annealing (800 K) cycles. Here, 40 monolayers (≈3.5 nm) of Co were deposited by electron beam evaporation epitaxy and annealed at a temperature of 600 K, leading to a hexagonal, bulklike Co structure with an in-plane magnetic uniaxial anisotropy along the high-symmetry axis of Co [72]. For the deposition of first- and second-layer Alq_3 molecules (in total 1.3 nm), we used a Knudsen cell and a quartz crystal balance calibrated with ellipsometry to monitor deposition rates. The *in situ* preparation of the sample leads to reproducible interfaces and all obtained experimental results were reproduced on multiple samples prepared, as described above.

B. Experimental method

We used femtosecond laser pulses from a Ti : Sapphire oscillator (Mai Tai, Spectra-Physics GmbH) to emit electrons from the sample. Photoelectrons were detected by TR-PEEM (IS-PEEM, Focus GmbH) [73]. The PEEM signal was spatially averaged over the imaged field of view ($30 \times 30\ \mu m^2$) to maximize the signal-to-noise ratio. No local differences of the PEEM signal were detected within the observed field of view. Spin-integrated and kinetic-energy-resolved PEEM images were obtained with a ToF-DLD with a typical energy resolution of 70 meV [49]. For all time-resolved experiments, we overlapped a pump pulse (400 nm, 3.1 eV) with the first pulse of a sequence of four probe pulses (800 nm, 1.55 eV, 55 fs) that were directed collinearly onto the surface. For this purpose, the beam path of the fundamental laser pulse was split into two arms. Frequency doubling of the fundamental laser radiation (800 nm) in a β-$BaBO_3$ crystal generated the 400 nm pump pulse. A home-built liquid-crystal-based pulse shaper created the pulse sequence in the other arm [74]. The pulse shaper enabled control of the relative phases and time delays between the probe pulses, while the relative phases between the 800 and 400 nm pulses were not stabilized. The probe pulses were fully characterized using frequency-resolved optical gating in combination with spectral interferometry [75,76]. The laser spot size of the 800 nm fundamental beam and the frequency-doubled 400 nm beam exhibited a size larger than the field of view so that the corresponding maximum fluence in the power-dependent yield measurements roughly amounts to values $< 1.0 \times 10^{-4}$ J cm^{-2} (75 mW beam power) and 1.4×10^{-6} J cm^{-2} (1 mW beam power), respectively.

In all-optical 2D spectroscopy, the RTG signal reveals the coherence evolution in a system [59]. The same is true for our collinear arrangement, with the only difference that we use phase cycling [58] to filter the photoemission contribution that is linked with the state populated by the interaction with the second pulse after the time interval τ. The same signal also comprises weaker higher-order contributions in which the second pulse immediately places the system back into the same coherence established by the first pulse, and after a second time interval t, the system is then again switched to a population state by the third pulse of the sequence. The coherence decay, and hence the dephasing time T_2, is probed during both time intervals.

For coherent optical 2D photoelectron spectroscopy, the local electron yield was recorded as a function of the time delays τ, T, and t and relative phases $\varphi_\tau = \varphi_2 - \varphi_1$, $\varphi_T = \varphi_3 - \varphi_2$, and $\varphi_t = \varphi_4 - \varphi_3$ between the four different probe pulses. With $T = 0$ fs and $\varphi_T = 0$ for all experimental data shown here, the pulse sequence effectively consisted of three pulses. Time delays τ and t, according to Fig. 2(a), were varied from 0 to 192 fs in steps of 8 fs. A $1 \times 3 \times 4 = 12$-fold RTG-equivalent phase-cycling scheme [58,59] extracted the coherence information from the total measurement signal, i.e., for each time-delay step, the kinetic-energy-resolved (energy E_{kin}) PEEM measurement was repeated for 12 different phase combinations of φ_τ and φ_t (with $\varphi_T = 0$), and the coherent signal $S_{RTG}(\tau, t, E_{kin})$ was obtained from the various photoelectron yields $Y_{el}(\tau, t, \varphi_\tau, \varphi_t, E_{kin})$ via

$$\begin{aligned} S_{RTG}(\tau,t,E_{kin}) = \tfrac{1}{12}\big\{ & Y_{el}(\tau,t,0,0,E_{kin}) + iY_{el}(\tau,t,0,\pi/2,E_{kin}) - Y_{el}(\tau,t,0,\pi,E_{kin}) - iY_{el}(\tau,t,0,3\pi/2,E_{kin}) \\ & + Y_{el}(\tau,t,2\pi/3,-2\pi/3,E_{kin}) + iY_{el}(\tau,t,2\pi/3,-\pi/6,E_{kin}) - Y_{el}(\tau,t,2\pi/3,\pi/3,E_{kin}) \\ & - iY_{el}(\tau,t,2\pi/3,5\pi/6,E_{kin}) + Y_{el}(\tau,t,4\pi/3,-4\pi/3,E_{kin}) + iY_{el}(\tau,t,4\pi/3,-5\pi/6,E_{kin}) \\ & - Y_{el}(\tau,t,4\pi/3,-\pi/3,E_{kin}) - iY_{el}(\tau,t,4\pi/3,\pi/6,E_{kin})\big\}. \end{aligned} \tag{2}$$

A 2D Fourier transform of $S_{\mathrm{RTG}}(\tau, t, E_{\mathrm{kin}})$ with respect to τ and t then led to the complex-valued kinetic-energy-resolved 2D spectra $S_{\mathrm{RTG}}(\hbar\omega_\tau, \hbar\omega_t, E_{\mathrm{kin}})$, with a spectral resolution along the optical axes of ≈22 meV that corresponds to the size of the pixels in Fig. 3(c), i.e., no zero padding was applied. The absolute-valued part of $S_{\mathrm{RTG}}(\hbar\omega_\tau, \hbar\omega_t, E_{\mathrm{kin}})$ is shown in Figs. 2(b) and 3(c) in this paper. For contour lines and isosurfaces, 11-fold zero padding was applied to $S_{\mathrm{RTG}}(\tau, t, E_{\mathrm{kin}})$ before Fourier transformation.

C. Quantum dynamical simulations

For the simulations of the model in Fig. 3(b), we numerically solved the Lindblad quantum master equation [77]:

$$\frac{\partial}{\partial t'}\rho(t') = -\frac{i}{\hbar}[\mathcal{H}(t'), \rho(t')] + \sum_n \frac{1}{T_n}\Big[J_n\rho(t')J_n^\dagger - \frac{1}{2}J_n^\dagger J_n\rho(t') - \frac{1}{2}\rho(t')J_nJ_n^\dagger\Big]. \quad (3)$$

In the Lindblad formalism, the Liouville–von Neumann equation, which describes the time evolution of the density matrix $\rho(t')$ under the Hamiltonian $H(t')$, is extended with additive terms that comprise relaxation and dephasing processes induced by the interaction of the quantum system with the environment. In Eq. (3), depending on the quantum jump operator J_n, T_n either denotes the time constant of an inelastic population relaxation, i.e., T_n corresponds to the population relaxation lifetime T_1, or is attributed to the pure dephasing time T_2^*. Here, $H(t')$ is the sum of the time-independent Hamiltonian:

$$\mathcal{H}_0 = \hbar\omega_m \sum_m |m\rangle\langle m|, \quad (4)$$

in energy eigenstate basis $\{|m\rangle\}$ with eigenenergies $\hbar\omega_m$, and the interaction Hamiltonian:

$$\mathcal{H}_I(t') = E(t)\sum_{m\neq n}\mu_{m,n}(|m\rangle\langle n| + |n\rangle\langle m|), \quad (5)$$

with $m, n \in \{\mathrm{HIS0}, \mathrm{HIS_F}, \mathrm{HIS1}, \mathrm{PE}, 1, 2, 3\}$, the driving laser field $E(t)$, and identical transition dipole moments $\mu_{m,n} =$ 0.08 a.u. assumed for all transitions.

The density matrix evolution was calculated from $t' = 0$ fs to $t'_{\mathrm{max}} = 700$ fs in steps of $\delta t' = 0.1$ fs in the rotating frame of the 800 nm probe pulses. The external fields were defined as

$$E(t', \Delta t) = E_0 \exp\Big[-2\log(2)\frac{(t'-\Delta t)^2}{\delta^2}\Big]\exp(i\omega_0 t' + i\varphi), \quad (6)$$

for the pump ($\hbar\omega_0 = 3.1$ eV, $\delta = 30$ fs, $E_0 = 5\times10^{-3}$ a.u., $\Delta t = 0$ fs) and probe pulses ($\hbar\omega_0 = 1.55$ eV, $\delta = 50$ fs, $E_0 = 5\times10^{-3}$ a.u., and the respective time delay Δt). The dipole moments $\mu_{m,n}$ were chosen such that only a small depopulation (<10%) of the ground states of the subsystems occurred to avoid saturation effects such as Rabi cycles. A detailed description of the assumed transition pathways is given in the Supplemental Material [64].

For the model in Fig. 3(b) (solid arrows), we represented the states in the first-layer Alq_3 subsystem as a four-level system and the second-layer Alq_3 subsystem as a three-level system which led to a 12 × 12-dimensional density matrix. The energy levels were $E(|\mathrm{HIS0}\rangle) = -1.60$ eV, $E(|\mathrm{HIS_F}\rangle) =$ 0 eV, $E(|\mathrm{X}\rangle) = 3.10$ eV, and $E(|\mathrm{PE}\rangle) = 4.65$ eV for the first-layer Alq_3 system and $\mathrm{E}(|1\rangle) = 1.50$ eV, $E(|2\rangle) = 3.01$ eV, and $E(|3\rangle) = 3.09$ eV for the second-layer Alq_3 system. Here, $|\mathrm{HIS0}\rangle$, $\langle\mathrm{HIS_F}\rangle$, $|\mathrm{HIS1}\rangle$, and $|\mathrm{X}\rangle$ denote the Co + first-layer Alq_3 hybridized states, $|\mathrm{PE}\rangle$ the photoemission state, and $|1\rangle$, $|2\rangle$, and $|3\rangle$ second-layer Alq_3 states. In the simulations, we assumed that the Auger-like process occurs via a unidirectional energy transfer between the second and the first Alq_3 layer. Note that the alternative, i.e., a transfer to neighboring excited molecules in the second layer, is only a change of names but does not affect the outcome of the simulation. Absolute energy differences $E(|2\rangle) - E(|1\rangle) = 1.51$ eV and $E(|3\rangle) - E(|1\rangle) = 1.59$ eV were taken from the result of a phenomenological fitting (see Supplemental Material [64]). Unidirectional energy transfer from the second-layer Alq_3 to the substrate subsystem was modeled using population-lowering operators in the second layer and raising operators in the substrate subsystem, while the total population was conserved (see Supplemental Material [64]). The large number of states and related free model parameters and the time for simulating a full 2D spectrum of ≈3.5 h makes a full fit of the model to the experimental data unfeasible. Hence, to find an optimized set of parameters, the population relaxation times $T_1(|\mathrm{X}\rangle)$, $T_1(|1\rangle)$, $T_1(|2\rangle)$, and $T_1(|3\rangle)$ were modified by hand, while the ratio $T_1(|2\rangle)/T_1(|3\rangle)$ was kept constant. The best parameter set out of 20 different sets was found by evaluating root-mean-square deviation of the diagonal of the simulated 2D spectrum from the diagonal of the experimental 2D spectrum. Short pure dephasing times in the Co system of $T_2^*(|\mathrm{HIS1}\rangle) = 0.1$ fs and $T_2^*(|\mathrm{PE}\rangle) = 0.1$ fs accounted for the metal character of the substrate and for a state above the vacuum potential, respectively, leading effectively to rate terms in the master equation for the corresponding transitions. Finally, the electron yield was determined by the population of the $|\mathrm{PE}\rangle$ state which served as a container, i.e., the population relaxation time was $T_1(|\mathrm{PE}\rangle) \to \infty$.

ACKNOWLEDGMENTS

This paper was supported by the German Science Foundation within the SPP 1839 (M.A., T.B., and W.P.) and the GSC 266 (P.T. and B.S.) and by the European Research Council within Consolidator Grant "MULTISCOPE"—Grant No. 614623 (T.B.) and within Consolidator Grant "hyControl"—Grant No. 725767 (M.C. and S.P). We acknowledge discussions with Pavel Malý.

The author list is in alphabetical order. M.A., T.B., M.C., B.S., and W.P. initiated and supervised the work. M.F., N.H., M.H., B.H., J.K., C.K., and P.T. performed the experiments. M.A., T.B., M.C., M.H., B.H., T.K., C.K., W.P., M.F., B.S., and P.T. developed the electron emission models. T.K. developed the Matlab simulation toolbox used for data modeling with contributions from B.H., who performed the simulations. All authors contributed to manuscript preparation.

[1] Y. Tanimura and S. Mukamel, Two-dimensional femtosecond vibrational spectroscopy of liquids, J. Chem. Phys. **99**, 9496 (1993).

[2] L. Lepetit and M. Joffre, Two-dimensional nonlinear optics using Fourier-transform spectral interferometry, Opt. Lett. **21**, 564 (1996).

[3] J. D. Hybl, A. W. Albrecht, S. M. Gallagher Faeder, and D. M. Jonas, Two-dimensional electronic spectroscopy, Chem. Phys. Lett. **297**, 307 (1998).

[4] P. Hamm, M. Lim, and R. M. Hochstrasser, Structure of the amide I band of peptides measured by femtosecond nonlinear-infrared spectroscopy, J. Phys. Chem. B **102**, 6123 (1998).

[5] H. S. Chung, Z. Ganim, K. C. Jones, and A. Tokmakoff, Transient 2D IR spectroscopy of ubiquitin unfolding dynamics, Proc. Natl. Acad. Sci. U.S.A. **104**, 14237 (2007).

[6] D. B. Strasfeld, Y. L. Ling, S.-H. Shim, and M. T. Zanni, Tracking fiber formation in human islet amyloid polypeptide with automated 2D-IR spectroscopy, J. Am. Chem. Soc. **130**, 6698 (2008).

[7] S.-H. Shim, R. Gupta, Y. L. Ling, D. B. Strasfeld, D. P. Raleigh, and M. T. Zanni, Two-dimensional IR spectroscopy and isotope labeling defines the pathway of amyloid formation with residue-specific resolution, Proc. Natl. Acad. Sci. U.S.A. **106**, 6614 (2009).

[8] S. Woutersen, Y. Mu, G. Stock, and P. Hamm, Hydrogen-bond lifetime measured by time-resolved 2D-IR spectroscopy: N-methylacetamide in methanol, Chem. Phys. **266**, 137 (2001).

[9] T. Brixner, T. Mančal, I. V. Stiopkin, and G. R. Fleming, Phase-stabilized two-dimensional electronic spectroscopy, J. Chem. Phys. **121**, 4221 (2004).

[10] Y. Song, S. N. Clafton, R. D. Pensack, T. W. Kee, and G. D. Scholes, Vibrational coherence probes the mechanism of ultrafast electron transfer in polymer-fullerene blends, Nat. Commun. **5**, 4933 (2014).

[11] S. M. Falke, C. A. Rozzi, D. Brida, M. Maiuri, M. Amato, E. Sommer, A. De Sio, A. Rubio, G. Cerullo, E. Molinari, and C. Lienau, Coherent ultrafast charge transfer in an organic photovoltaic blend, Science **344**, 1001 (2014).

[12] A. De Sio, F. Troiani, M. Maiuri, J. Réhault, E. Sommer, J. Lim, S. F. Huelga, M. B. Plenio, C. A. Rozzi, G. Cerullo, E. Molinari, and C. Lienau, Tracking the coherent generation of polaron pairs in conjugated polymers, Nat. Commun. **7**, 13742 (2016).

[13] T. Brixner, J. Stenger, H. M. Vaswani, M. Cho, R. E. Blankenship, and G. R. Fleming, Two-Dimensional spectroscopy of electronic couplings in photosynthesis, Nature (London) **434**, 625 (2005).

[14] J. Dostál, J. Pšenčík, and D. Zigmantas, *In situ* mapping of the energy flow through the entire photosynthetic apparatus, Nat. Chem. **8**, 705 (2016).

[15] T. Brixner, R. Hildner, J. Köhler, C. Lambert, and F. Würthner, Exciton transport in molecular aggregates—from natural antennas to synthetic chromophore systems, Adv. Energy Mater. **7**, 1700236 (2017).

[16] J. Cao, R. J. Cogdell, D. F. Coker, H.-G. Duarn, J. Hauer, U. Kleinekathöfer, T. L. C. Jansen, T. Mančal, R. J. D. Miller, J. P. Ogilvie, V. I. Prokhorenko, T. Renger, H.-S. Tan, R. Tempelaar, M. Thorwart, E. Thyrhaug, S. Westenhoff, and D. Zigmantas, Quantum biology revisited, Sci. Adv. **6**, eaaz4888 (2020).

[17] S. Ruetzel, M. Diekmann, P. Nuernberger, C. Walter, B. Engels, and T. Brixner, Multidimensional spectroscopy of photoreactivity, Proc. Natl. Acad. Sci. U.S.A. **111**, 4764 (2014).

[18] P. Nuernberger, S. Ruetzel, and T. Brixner, Multidimensional electronic spectroscopy of photochemical reactions, Angew. Chem. Int. Ed. **54**, 11368 (2015).

[19] M. Cho, *Two-Dimensional Optical Spectroscopy* (CRC Press, Boca Raton, 2009).

[20] M. D. Fayer, *Ultrafast Infrared Vibrational Spectroscopy*, 1st ed. (CRC Press, Boca Raton, 2013).

[21] W. Kuehn, K. Reimann, M. Woerner, T. Elsaesser, and R. Hey, Two-dimensional terahertz correlation spectra of electronic excitations in semiconductor quantum wells, J. Phys. Chem. B **115**, 5448 (2011).

[22] S. M. Teo, B. K. Ofori-Okai, C. A. Werley, and K. A. Nelson, Invited Article: Single-shot THz detection techniques optimized for multidimensional THz spectroscopy, Rev. Sci. Instrum. **86**, 051301 (2015).

[23] C.-H. Tseng, S. Matsika, and T. C. Weinacht, Two-dimensional ultrafast Fourier transform spectroscopy in the deep ultraviolet, Opt. Express **17**, 18788 (2009).

[24] U. Selig, C.-F. Schleussner, M. Foerster, F. Langhojer, P. Nuernberger, and T. Brixner, Coherent two-dimensional ultraviolet spectroscopy in fully noncollinear geometry, Opt. Lett. **35**, 4178 (2010).

[25] S. Mukamel, D. Healion, Y. Zhang, and J. D. Biggs, Multidimensional attosecond resonant x-ray spectroscopy of molecules: Lessons from the optical regime, Annu. Rev. Phys. Chem. **64**, 101 (2013).

[26] M. Cho, H. M. Vaswani, T. Brixner, J. Stenger, and G. R. Fleming, Exciton analysis in 2D electronic spectroscopy, J. Phys. Chem. B **109**, 10542 (2005).

[27] J. M. Anna, Y. Song, R. Dinshaw, and G. D. Scholes, Two-dimensional electronic spectroscopy for mapping molecular photophysics, Pure Appl. Chem. **85**, 1307 (2013).

[28] E. Thyrhaug, R. Tempelaar, M. J. P. Alcocer, K. Žídek, D. Bína, J. Knoester, T. L. C. Jansen, and D. Zigmantas, Identification and characterization of diverse coherences in the Fenna-Matthews-Olson complex, Nat. Chem. **10**, 780 (2018).

[29] S. Sanvito, Molecular spintronics: The rise of spinterface science, Nat. Phys. **6**, 562 (2010).

[30] C. Barraud, P. Seneor, R. Mattana, S. Fusil, K. Bouzehouane, C. Deranlot, P. Graziosi, L. Hueso, I. Bergenti, V. Dediu, F. Petroff, and A. Fert, Unravelling the role of the interface for spin injection into organic semiconductors, Nat. Phys. **6**, 615 (2010).

[31] M. Cinchetti, V. A. Dediu, and L. E. Hueso, Activating the molecular spinterface, Nat. Mater. **16**, 507 (2017).

[32] J. Bredenbeck, A. Ghosh, H.-K. Nienhuys, and M. Bonn, Interface-specific ultrafast two-dimensional vibrational spectroscopy, Acc. Chem. Res. **42**, 1332 (2009).

[33] W. Xiong, J. E. Laaser, R. D. Mehlenbacher, and M. T. Zanni, Adding a dimension to the infrared spectra of interfaces using heterodyne detected 2D sum-frequency generation (HD 2D SFG) spectroscopy, Proc. Natl. Acad. Sci. U.S.A. **108**, 20902 (2011).

[34] Z. Zhang, L. Piatkowski, H. J. Bakker, and M. Bonn, Ultrafast vibrational energy transfer at the water/air interface revealed by two-dimensional surface vibrational spectroscopy, Nat. Chem. **3**, 888 (2011).

[35] J. P. Kraack, D. Lotti, and P. Hamm, 2D attenuated total reflectance infrared spectroscopy reveals ultrafast vibrational dynamics of organic monolayers at metal-liquid interfaces, J. Chem. Phys. **142**, 212413 (2015).

[36] C. Yan, R. Yuan, W. C. Pfalzgraff, J. Nishida, L. Wang, T. E. Markland, and M. D. Fayer, Unraveling the dynamics and structure of functionalized self-assembled monolayers on gold using 2D IR spectroscopy and MD simulations, Proc. Natl. Acad. Sci. U.S.A. **113**, 4929 (2016).

[37] V. A. Dediu, L. E. Hueso, I. Bergenti, and C. Taliani, Spin routes in organic semiconductors, Nat. Mater. **8**, 707 (2009).

[38] H. Petek and S. Ogawa, Femtosecond time-resolved two-photon photoemission studies of electron dynamics in metals, Prog. Surf. Sci. **56**, 239 (1997).

[39] S. Ogawa, H. Nagano, and H. Petek, Phase and Energy Relaxation in an Antibonding Surface State: Cs/Cu(111), Phys. Rev. Lett. **82**, 1931 (1999).

[40] M. Reutzel, A. Li, and H. Petek, Coherent Two-Dimensional Multiphoton Photoelectron Spectroscopy of Metal Surfaces, Phys. Rev. X **9**, 011044 (2019).

[41] D. Uhl, U. Bangert, L. Bruder, and F. Stienkemeier, Coherent optical 2D photoelectron spectroscopy, Optica **8**, 1316 (2021).

[42] P. Tian, D. Keusters, Y. Suzaki, and W. S. Warren, Femtosecond phase-coherent two-dimensional spectroscopy, Science **300**, 1553 (2003).

[43] P. F. Tekavec, G. A. Lott, and A. H. Marcus, Fluorescence-detected two-dimensional electronic coherence spectroscopy by acousto-optic phase modulation, J. Chem. Phys. **127**, 214307 (2007).

[44] S. Draeger, S. Roeding, and T. Brixner, Rapid-scan coherent 2D fluorescence spectroscopy, Opt. Express **25**, 3259 (2017).

[45] V. Tiwari, Y. A. Matutes, A. T. Gardiner, T. L. C. Jansen, R. J. Cogdell, and J. P. Ogilvie, Spatially-resolved fluorescence-detected two-dimensional electronic spectroscopy probes varying excitonic structure in photosynthetic bacteria, Nat. Commun. **9**, 4219 (2018).

[46] D. Ino, K. Watanabe, N. Takagi, and Y. Matsumoto, Electronic structure and femtosecond electron transfer dynamics at noble metal/tris-(8-hydroxyquinoline) aluminum interfaces, Phys. Rev. B **71**, 115427 (2005).

[47] C.-K. Min, Y. Lee, Y. Park, and J. W. Kim, Interface electronic structure and dynamics of tris-(8-hydroxyquinoline) aluminum on Cu(100), New J. Phys. **11**, 103011 (2009).

[48] A. Droghetti, P. Thielen, I. Rungger, N. Haag, N. Großmann, J. Stöckl, B. Stadtmüller, M. Aeschlimann, S. Sanvito, and M. Cinchetti, Dynamic spin filtering at the Co/Alq_3 interface mediated by weakly coupled second layer molecules, Nat. Commun. **7**, 12668 (2016).

[49] S. Steil, N. Großmann, M. Laux, A. Ruffing, D. Steil, M. Wiesenmayer, S. Mathias, O. L. A. Monti, M. Cinchetti, and M. Aeschlimann, Spin-dependent trapping of electrons at spinterfaces, Nat. Phys. **9**, 242 (2013).

[50] M. D. Halls and H. B. Schlegel, Molecular orbital study of the first excited state of the OLED material tris(8-hydroxyquinoline)aluminum(III), Chem. Mater. **13**, 2632 (2001).

[51] S. Krause, M. B. Casu, A. Schöll, and E. Umbach, Determination of transport levels of organic semiconductors by UPS and IPS, New J. Phys. **10**, 085001 (2008).

[52] B. Stadtmüller, S. Emmerich, D. Jungkenn, N. Haag, M. Rollinger, S. Eich, M. Maniraj, M. Aeschlimann, M. Cinchetti, and S. Mathias, Strong modification of the transport level alignment in organic materials after optical excitation, Nat. Commun. **10**, 1470 (2019).

[53] A. Oelsner, M. Rohmer, C. Schneider, D. Bayer, G. Schönhense, and M. Aeschlimann, Time- and energy resolved photoemission electron microscopy-imaging of photoelectron time-of-flight analysis by means of pulsed excitations, J. Electron Spectrosc. Relat. Phenom. **178–179**, 317 (2010).

[54] M. Aeschlimann, T. Brixner, A. Fischer, C. Kramer, P. Melchior, W. Pfeiffer, C. Schneider, C. Strüber, P. Tuchscherer, and D. V. Voronine, Coherent two-dimensional nanoscopy, Science **333**, 1723 (2011).

[55] M. Aeschlimann, T. Brixner, D. Differt, U. Heinzmann, M. Hensen, C. Kramer, F. Lükermann, P. Melchior, W. Pfeiffer, M. Piecuch, C. Schneider, H. Stiebig, C. Strüber, and P. Thielen, Perfect absorption in nanotextured thin films via Anderson-localized photon modes, Nat. Photonics **9**, 663 (2015).

[56] B. Huber, S. Pres, E. Wittmann, L. Dietrich, J. Lüttig, D. Fersch, E. Krauss, D. Friedrich, J. Kern, V. Lisinetskii, M. Hensen, B. Hecht, R. Bratschitsch, E. Riedle, and T. Brixner, Space- and time-resolved UV-to-NIR surface spectroscopy and 2D nanoscopy at 1 MHz repetition rate, Rev. Sci. Instrum. **90**, 113103 (2019).

[57] M. Dąbrowski, Y. Dai, and H. Petek, Ultrafast photoemission electron microscopy: Imaging plasmons in space and time, Chem. Rev. **120**, 6247 (2020).

[58] H.-S. Tan, Theory and phase-cycling scheme selection principles of collinear phase coherent multi-dimensional optical spectroscopy, J. Chem. Phys. **129**, 124501 (2008).

[59] E. J. Brown, Q. Zhang, and M. Dantus, Femtosecond transient-grating techniques: Population and coherence dynamics involving ground and excited states, J. Chem. Phys. **110**, 5772 (1999).

[60] S. Goetz, D. Li, V. Kolb, J. Pflaum, and T. Brixner, Coherent two-dimensional fluorescence micro-spectroscopy, Opt. Express **26**, 3915 (2018).

[61] P. Malý, J. Lüttig, S. Mueller, M. H. Schreck, C. Lambert, and T. Brixner, Coherently and fluorescence-detected two-dimensional electronic spectroscopy: Direct comparison on squaraine dimers, Phys. Chem. Chem. Phys. **22**, 21222 (2020).

[62] P. Malý and T. Mančal, Signatures of exciton delocalization and exciton-exciton annihilation in fluorescence-detected two-dimensional coherent spectroscopy, J. Phys. Chem. Lett. **9**, 5654 (2018).

[63] P. Malý, S. Mueller, J. Lüttig, C. Lambert, and T. Brixner, Signatures of exciton dynamics and interaction in coherently and fluorescence-detected four- and six-wave-mixing two-dimensional electronic spectroscopy, J. Chem. Phys. **153**, 144204 (2020).

[64] See Supplemental Material at http://link.aps.org/supplemental/10.1103/PhysRevB.105.205415 for power-law experiments, pump-probe experiments with two-probe-pulse sequencies, pathways of simulated photoemission models, and phenomenological fitting procedure.

[65] V. Blanchet, M. Z. Zgierski, T. Seideman, and A. Stolow, Discerning vibronic molecular dynamics using time-resolved photoelectron spectroscopy, Nature (London) **401**, 52 (1999).

[66] M. Schmitt, S. Lochbrunner, J. P. Shaffer, J. J. Larsen, M. Z. Zgierski, and A. Stolow, Electronic continua in time-resolved

photoelectron spectroscopy. II. Corresponding ionization correlations, J. Chem. Phys. **114**, 1206 (2001).

[67] T. Jahnke, U. Hergenhahn, B. Winter, R. Dörner, U. Frühling, P. V. Demekhin, K. Gokhberg, L. S. Cederbaum, A. Ehresmann, A. Knie, and A. Dreuw, Interatomic and intermolecular coulombic decay, Chem. Rev. **120**, 11295 (2020).

[68] M. Aeschlimann, M. Bauer, S. Pawlik, W. Weber, R. Burgermeister, D. Oberli, and H. C. Siegmann, Ultrafast Spin-Dependent Electron Dynamics in Fcc Co, Phys. Rev. Lett. **79**, 5158 (1997).

[69] A. Curioni, M. Boero, and W. Andreoni, Alq_3: *ab initio* calculations of its structural and electronic properties in neutral and charged states, Chem. Phys. Lett. **294**, 263 (1998).

[70] M. Brinkmann, G. Gadret, M. Muccini, C. Taliani, N. Masciocchi, and A. Sironi, Correlation between molecular packing and optical properties in different crystalline polymorphs and amorphous thin films of mer-tris(8-hydroxyquinoline)aluminum(III), J. Am. Chem. Soc. **122**, 5147 (2000).

[71] V. Butkus, L. Valkunas, and D. Abramavicius, Vibronic phenomena and exciton-vibrational interference in two-dimensional spectra of molecular aggregates, J. Chem. Phys. **140**, 034306 (2014).

[72] N. Haag, M. Laux, J. Stöckl, J. Kollamana, J. Seidel, N. Großmann, R. Fetzer, L. L. Kelly, Z. Wei, B. Stadtmüller, M. Cinchetti, and M. Aeschlimann, Epitaxial growth of thermally stable cobalt films on Au(111), New J. Phys. **18**, 103054 (2016).

[73] O. Schmidt, M. Bauer, C. Wiemann, R. Porath, M. Scharte, O. Andreyev, G. Schönhense, and M. Aeschlimann, Time-resolved two photon photoemission electron microscopy, Appl. Phys. B Lasers Opt. **74**, 223 (2002).

[74] A. M. Weiner, Femtosecond pulse shaping using spatial light modulators, Rev. Sci. Instrum. **71**, 1929 (2000).

[75] R. Trebino, *Frequency-Resolved Optical Gating: The Measurement of Ultrashort Laser Pulses* (Springer, New York, 2002).

[76] L. Lepetit, G. Chériaux, and M. Joffre, Linear techniques of phase measurement by femtosecond spectral interferometry for applications in spectroscopy, J. Opt. Soc. Am. B Opt. Phys. **12**, 2467 (1995).

[77] G. Lindblad, On the generators of quantum dynamical semigroups, Commun. Math. Phys. **48**, 119 (1976).